Revealing the (positive) role of porosity within polymeric additively manufactured lattices via X-ray computed tomography

International Journal of Solids and Structures 320 (2025) 113488

Contents lists available at ScienceDirect

International Journal of Solids and Structures

journal homepage: www.elsevier.com/locate/ijsolstr

Revealing the (positive) role of porosity within polymeric additively manufactured lattices via X-ray computed tomography

Danilo Bruson [a,*], Itziar Serrano-Munoz [b], Tobias Fritsch [b], Henning Markötter [b], Manuela Galati [a]

[a] Department of Management and Production Engineering, Corso Duca degli Abruzzi 24, 10129 Turin, Italy
[b] Bundesanstalt für Materialforschung und -prüfung (BAM), Unter den Eichen 87, 12205 Berlin, Germany

ARTICLE INFO

Keywords:
Nylon Pa2200
Laser powder bed fusion (PBF-LB)
Processing defects
Synchrotron X-ray computed tomography (XCT)
Digital volume correlation (DVC)
Image-based finite element simulations

ABSTRACT

The mechanical properties of lattice geometries are known to be significantly influenced by a variety of manufacturing defects. This study investigates the influence of porosity on the mechanical behaviour of strut-based body-centred cubic (BCC) lattice structures produced with powder bed fusion with laser beam PBF-LB/P using PA2200 nylon powder. The study combines advanced techniques, including in-situ laboratory X-ray computed tomography (XCT), synchrotron XCT to visualise pores and roughness in high resolution at a single-cell level and image-based finite element analysis (FEA). The findings show that failure in thin-walled AM lattices is governed by the combined effects of porosity morphology, location, surface roughness, and cross-section reduction. The presence of internal porosity is found to attenuate both the amplitude of elastic modulus fluctuations and the severity of stress concentrations induced by surface irregularities.

1. Introduction

The recent advancements in additive manufacturing (AM) technologies have resulted in a significant increase in the number of applications of functional manufacturing (González-Henríquez et al., 2019). The most prevalent AM technologies for polymers, particularly powder bed fusion with laser beam (PBF-LB) processes, are consistently attracting industrial attention due to their simplicity of part nesting, functional end-use parts, mass production, and the absence of support, even for complex geometries (Tan et al., 2020). Lattice structures are a distinctive geometrical feature that showcases the design flexibility enabled by the layer-by-layer production process (Giannitelli et al., 2014; Pan et al.). These structures are being implemented in response to the growing demand for lightweight components with custom stiffness. As the size of the manufactured features and the process's ability to maintain consistent quality in terms of porosity and geometry are reduced, the quality of PBF-LB parts becomes more critical. This is because a significant variation in these characteristics would alter the mechanical response of manufactured parts, resulting in a deviation from the design requirements (Pavan et al., 2016).

The literature is unanimous in asserting that the varying sizes, thicknesses, orientations, and relative positions of small cylindrical elements or thin sheets within the building chamber, typically found in lightweight structures, could result in varying material properties, leading to varying mechanical strengths. When designing structures of this nature for end-use applications, it is crucial to consider these variables (Pavan et al., 2016; Sindinger et al., 2020; Liebrich et al., 2019; Tasch et al., 2018; Viccica et al., 2022). It is well established that PBF-LB processing of polymers relies on partial sintering, leading to uniformly distributed porosities in bulk components. In thin reticular structures, small pores also remain uniformly distributed along the struts, while nodes may exhibit porosity clustering (Bruson et al., 2023). Although porosity in bulk components results in brittle material behaviour (Calignano et al., 2021), combining defects and extremely thin structures on the material's deformation mechanisms remains poorly understood, particularly in the case of polymers. On the contrary, the research on this aspect is growing in the case of metallic materials (Červinek et al., 2021; Dressler et al., 2019; della Ventura et al., 2024; Suard et al., 2015; Sombatmai et al., 2021; Li et al., 2024; Somlo et al., 2022; Molavitabrizi et al., 2022) obtained through powder bed fusion processes. In Ref. (Lozanovski et al., 2020), the average stress concentration factor (SCF) associated with internal porosity in the nodes was found to be lower than 1, meaning a potential mitigating role of geometric artefacts and dimensional inaccuracies that behave as stress-

* Corresponding author.
E-mail address: danilo.bruson@polito.it (D. Bruson).

https://doi.org/10.1016/j.ijsolstr.2025.113488
Received 18 November 2024; Received in revised form 14 May 2025; Accepted 26 May 2025
Available online 3 June 2025

relieving fillets. This phenomenon may help explain why some small internal porosities do not immediately lead to failure, despite their presence. Also, failure could start at nodal junctions because the presence of porosity agglomeration reduces the effective load-bearing cross-section (Lozanovski et al., 2020). However, those results can hardly be extended, without verification, for the polymer because the process is based on a sintering process instead of fully melting (Han et al., 2022). Therefore, behind the pure properties of the material, the pore shape and distribution are significantly different.

This work investigated this effect using a strut-based body-centred cubic lattice topology. In-situ laboratory X-ray computed tomography (XCT) is used to evaluate the impact of defects on the tensile response of a PA2200 lattice structure manufactured via the PBF-LB technique. Synchrotron XCT is employed to acquire a high-definition visualisation of pores and roughness at the single cell level. The 3D volume reconstruction of a single vertical strut is used to perform an image-based finite element analysis (FEA) to be compared to an approximation which considers the modelling of the cross section of the strut as elliptical. The combination of XCT and FEA provides valuable insights of the deformation mechanism of the strut.

2. Materials and methods

2.1. Sample design and manufacturing

The body centred cubic (BCC) is a topology commonly applied and investigated in the literature (Bai et al., 2020; Gümrük and Mines, 2013; Leary et al., 2016; Porter et al., 2022; Maskery et al., 2015; Lei et al., 2019; Mazur et al., 2017). It is composed of four diagonal struts that are arranged along the diagonals of an ideal cube, forming a single central node in the cube centroid (Fig. 1 a)). The size of each strut was set equal to 1 mm, while the cell size was selected to fit two elementary cells in the thickness of a dog-bone specimen, which was set equal to 11 mm. Therefore, considering the strut diameter, the size of the elementary cell was equal to 5 mm, and the resulting relative density of the structure was equal to 25 %. The design of the tensile dog-bone specimen is reported in Fig. 1 b), in which five elementary cells are included in the gauge length, while the density graduation pattern has been operated out of the gauge length, according to Ref. (Bruson et al., 2023). Therefore, towards the bulk tabs of the sample, the final two cells exhibit an increase in strut diameter from 1 mm (gauge length constant density) to 1.44 mm and 2.08 mm. The two holes in each tab facilitate the sample's mounting.

The specimens were fabricated using PA2200 powder (polyamide 12 or PA12, with a mixture of 50 % virgin and 50 % recycled). Example of application of in industrial sectors are the fabrication of customized orthopaedic implants and devices (Păcurar et al., 2021; Lindberg et al., 2018) because the adequate compressive strength and suitability for load-bearing functions, motorsport sector because the demand for lightweight and structurally robust components (Sindinger et al., 2021; Marschall et al., 2020) has risen interest in the adoption of PA2200.

The production has been performed using an EOS Formiga P110 Velocis system laser, a powder bed fusion (PBF-LB) system. The process parameters were set as reported in Table 1 (Calignano et al., 2021). The samples were built in the edgewise configuration, thus with the sample thickness perpendicular to the build orientation (Z-axis). One specimen was used for in-situ testing, while another served as a comparison for the ex-situ testing results. An additional simplified specimen, including one single column of elementary cells, has been manufactured to acquire a high-definition visualisation of pores and roughness using synchrotron X-ray computed tomography (Fig. 1 (c)).

2.2. X-ray computed tomography (XCT)

2.2.1. In situ tensile loading

A DEBEN CT5000 tensile rig equipped with a 5 kN load cell was integrated into a laboratory GE v|tome|x L 180/300 system. The sample was fitted into the rig jaws by clamping its top and bottom grips be the use of two screws each. A load-controlled tension test was performed at a constant displacement rate of 0.1 mm/min. A first XCT scan corresponding to the as-built (i.e., undamaged state) was performed using a 5 N preload in order to prevent the sample from moving during the scan. Afterwards, the loading was interrupted at 400 N, 500 N and 600 N loads with a constant displacement. Prior to the XCT scans, an average of 20 min waiting time was needed to reach fully relaxation (Fig. 5 a)). The loading direction (Y axis in Fig. 3 a), c)) was perpendicular to the sample build direction. The sample was scanned at 60 kV and 250 μA for a total of 3001 projections over 360° with a 2024 × 2024 flat panel detector,

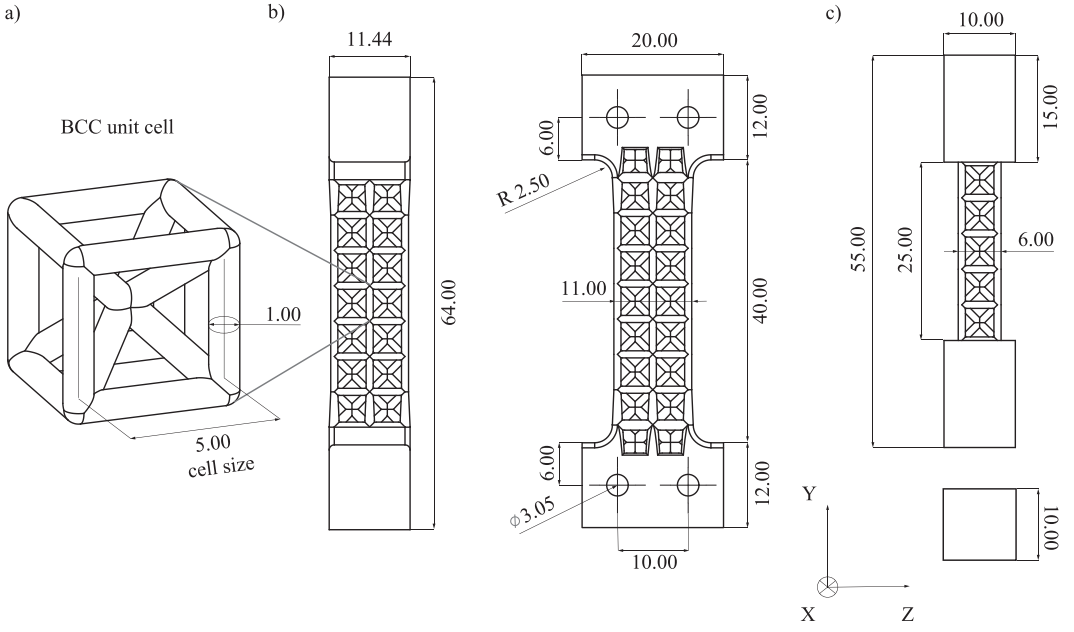

Fig. 1. a) Magnification of the bcc unit cell topology with a cell size of 5 mm, b) CAD drawing of the sample for both ex- and in-situ tests (64 mm total length) and c) CAD drawing of the sample geometry for synchrotron X-ray CT analysis. The Z axis of the reported manufacturing coordinate reference system represents the building direction.

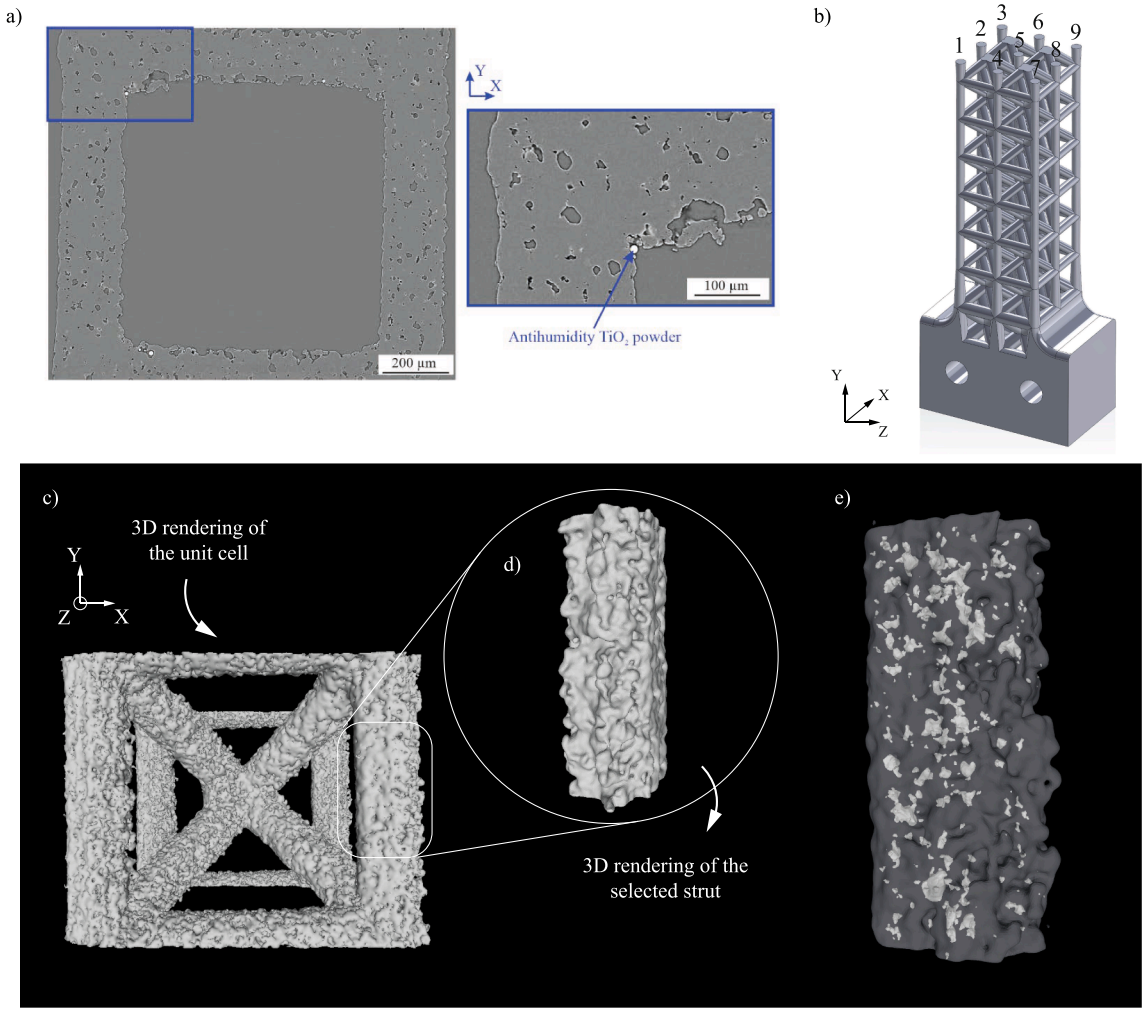

Fig. 2. a) XCT reconstructed tomogram of one of a BCC1 unit cell obtained using of the simplified lattice (Fig. 1 a). b) Numbering indexes of the longitudinal struts c) 3D rendering of the BCC1 unit cell. d) 3D detail representing one of the vertical struts. e) 3D detail of the internal defects contained within the selected strut.

Table 1
Number of nodes, elements and elapsed CPU time for the FE models.

Model	Nodes	Elements	CPU time [s]
CAD	84,275	56,333	227
Elliptic	8490	40,104	331
XCT reconstruction NP model	1,308,267	895,277	5438
XCT reconstruction P model	3,004,643	2,136,032	38,956

while using a 3 s exposure time per projection. The reconstructed voxel size was $12 \times 12 \times 12\ \mu m^3$. This allowed to visualise about 20 mm of the height (the total gauge length of the lattice height is 25 mm). The reconstruction was performed using a Feldkamp algorithm (Feldkamp et al., 1984).

2.2.2. *Quantitative image analysis*

The XCT data were first filtered using the non-local means (sigma 8 and smoothing factor 1, (Buades et al., 2011) filter available on Fiji software (Schindelin et al., 2012). The scans were subsequently loaded on Avizo software for segmentation (using the Otsu method (Otsu, 1979) and subsequent parametric study. A porosity analysis was performed on the segmented images to determine the 3D size of pores by means of the 3D equivalent diameter (EqD) of a sphere of the same volume. Only pores larger than EqD = 30 µm were considered to avoid false positive classification. Moreover, only internal pores were considered in the analysis, i.e., pores that interest the free surface of the lattice were considered as surface defects and accounted for in the thickness analysis. The geometric shape of pores was determined using the 3D Shape Factor, which equals 1 for a perfect sphere, while larger values indicate an object that is less compact. The thickness of the struts was computed by considering that each voxel represents the diameter of the largest sphere that contains the voxel and can be entirely inscribed with the closest boundaries of the analysed object (Hildebrand and Rüegsegger, 1997). Finally, the surface curvature was calculated using the 1/Max Curvature parameter (m^2), corresponding to the radius of a sphere locally fitting the surface.

For the roughness analysis, three struts with the longitudinal axis oriented parallel to Y-axis, parallel to X-axis, and the diagonal of the unit cell (Fig. 1) were analysed. These struts were located at the centre of the gauge, and their analysed length was about 2.2 mm. The surface roughness determination was performed with the advanced surface determination tool by VGStudio MAX 2023.2. The surface was exported as a triangulated surface mesh with the smallest element size of 12 µm. Line profiles along the length of each strut were extracted with a step size of 1° around the circumsphere of each strut. These line profiles were analysed according to the mean roughness profile parameter R_a. For more details, the reader can refer to Ref. (Fritsch et al., 2022).

The filtered XCT datasets were conditioned for digital volume correlation (DVC) by applying a binning of 2. The python-based open-source software SPAM (Stamati et al., 2020) was used to measure

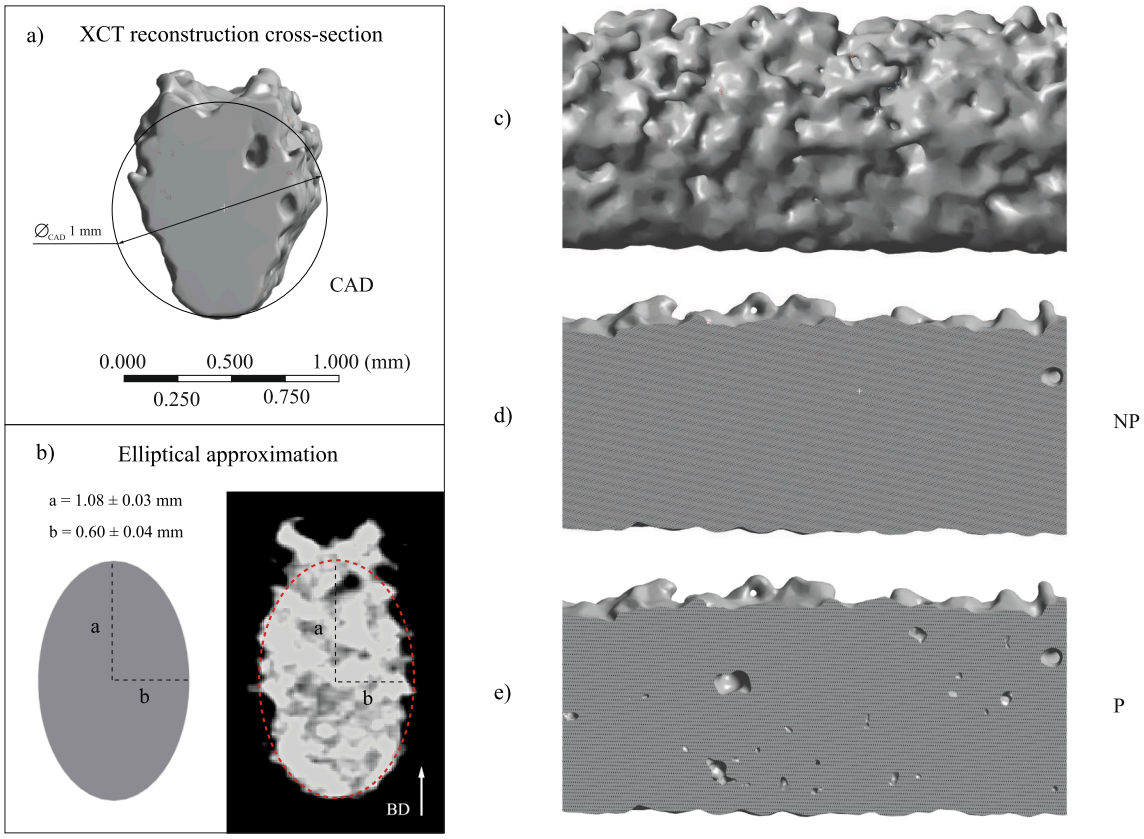

Fig. 3. a) Actual/nominal strut cross-section, b) elliptic cross-section approximation (Bruson et al., 2023) where BD refers to the build direction, c) detail of the reconstructed irregular actual surface, d-e) section views of the XCT reconstructed NP and P strut models.

displacement fields between images of a deforming specimen. The datasets obtained between 400 N and 500 N were projected onto a regular spaced grid. The mesh size is set to 16 voxels with a node spacing of 8 voxels. Strain fields are subsequently computed using the obtained displacement fields. For each quadrilateral element (Q8) of the mesh, a transformation gradient tensor F (as in $dx = FdX$) was calculated at the centre of the element using the displacement vectors of the corresponding nodes. Note that F provides richer information at the local scale than the displacement vector u alone since it considers the motion of a point with respect to its neighbours.

2.2.3. Synchrotron XCT

The synchrotron X-ray CT scan was performed at the imaging station of the BAMline (Rack et al., 2008; Markötter et al., 2022; Markötter et al., 2023) at the BESSY II synchrotron. To capture one unit cell of the sample, the 10x lens corresponding to a field of view of 9.2 × 7.8 mm^2 was chosen. This results in an effective pixel size of 3.6 μm, while the employed camera (sCMOS-type; PCO.edge-5.5) offers 2560 × 2160 pixels. A 150 μm thick $CdWO_4$ scintillator screen is combined with the 10x lens. 2500 projections, each with an exposure time of 150 ms, over an angular range of 180° were collected in on-the-fly mode, in which projections are collected during continuous rotation (see details in (Markötter et al., 2022). For an optimal signal-to-noise ratio, the double multilayer monochromator was facilitated at 20 keV, with a dE/E of approximately 3.5 %. Reconstruction was performed using in-house Python code based on Tomopy (Gürsoy et al., 2014) and astra toolbox (van Aarle et al., 2016). This synchrotron experiment is performed to a high-definition visualisation of roughness and pores, otherwise not achievable using laboratory X-ray sources. Note that a simplified lattice where the cross section only contains one unit cell was specifically printed for this purpose (see Fig. 2 a)).

2.3. Image-based finite element analysis (FEA)

The Nylon PA2200 material induces a low degree of contrast between the background and the lattice, as compared to other materials such as metals. The XCT images were first processed using a non-local means filter (sigma 8 and smoothing factor 1, (Buades et al., 2011) available on Fiji software (Schindelin et al., 2012). The segmentation was performed on Avizo software by using the Otsu's automatic global thresholding algorithm (Otsu, 1979). This segmentation excluded the unmolten anti-humidity TiO_2 powder (added by the supplier as an anti-humidity agent (Schmid, 2018) that remains trapped over the lattice surface (Fig. 2 a)). Fig. 2 b) shows the numbering of the longitudinal columns. The segmented dataset was subsequently processed to generate a microstructurally faithful surface mesh, where the surface roughness and porosity are represented in detail. The original surface generation yielded a surface mesh of about 60 million triangles and was iteratively simplified to about 2.5 million triangles, as shown in Fig. 2 d). This file was exported as an STL file for further processing. Fig. 2 (c), (d) shows the image-based 3D mesh (the edges of the triangles are not shown) of the entire cell-unit and the single strut (2.5 mm height), respectively. A 2.5 mm long single strut portion of the whole cell was selected for the numerical analysis. In addition, Fig. 2 (e) shows the case where the internal porosity is also included in the image-based 3D mesh (a transparent external shell is used to highlight the pores). The internal porosities and the characterisation are discussed in the Section 3.1 as a result of the in-situ testing.

As above mentioned, in order to investigate the role of process-related defects on the mechanical behaviour of a single strut, four distinct finite elements (FE) models with an increasing fidelity with respect to the real manufactured struts were considered: (a) the as-designed nominal CAD model, called "CAD"; (b) the approximated

CAD model, called "elliptic", utilising the equivalent elliptic cross-section derived by averaging the actual dimensions obtained from XCT; and the image-based mesh accounting for two different scenarios (c) considering only surface irregularities (named "NP") and (d) a fully reconstruction of the XCT data in a model that includes external irregularities and internal porosities (named "P). The length of the modelled strut is equal to 2.5 mm for all models. The extracted strut from the main structure is oriented with its main axis perpendicular to the build direction. This configuration was selected because it typically exhibits the poorest geometrical accuracy due to the layer-wise nature of the additive manufacturing process (Pavan et al., 2016; Bruson et al., 2023). As it can be observed in Fig. 3, this build orientation leads to a noticeable deviation from circularity in the real geometry (Fig. 3 (a)), resulting in an ovalised cross-section when compared to the nominal CAD model. The ovalisation of the struts is due to the production when building overhanging (unsupported) thin struts with the cylindrical axis perpendicular to the build direction (Pavan et al., 2016; Bruson et al., 2023). The first layers of scanned material lie on powder with a relatively poor thermal conductivity. This condition creates a local overheat and a heat flow along the build direction, which produces the typical ovalised section with the major axis of the ellipse parallel to the build direction (Fig. 3 (b)). The semi-axes of the elliptical cross-section used in the model (Fig. 3 (b), a = 1.08 ± 0.03 mm and b = 0.60 ± 0.04) were derived from a CT-scan-based experimental measurement campaign conducted on struts with the same geometry and orientation, as detailed in Ref. (Bruson et al., 2023). While the CAD model with 1 mm diameter was directly extracted from the CAD file of the designed geometry, elliptic model is therefore an ideal strut geometry with the same length but modelled with the elliptical cross-section that accounts for the geometrical process induced defect, according to Ref (Bruson et al., 2023)- Fig. 3 (c) displays the surface of the actual produced strut obtained by reconstructing the XCT with the typical irregularities due to the PBF-LB/P process as the partially sintered powder particles that stick on the surface (Pavan et al., 2016). Fig. 3 (d) reports the full-dense section view of the NP model, while accounting for the external irregularities on the strut surface. The external irregularities and internal porosities are instead considered in the P model in Fig. 3 (e), which is a high-fidelity reconstruction of the tomographic analysis. The morphological characterisation of the internal porosity is described in Section 3.1.

The aim of the numerical analysis is to conduct a comparative study evaluating the influence of different levels of geometric approximation, up to the full modelling of the actual strut geometry, including both external and internal porosities. The single strut is selected because it allows for a balance between reasonable computational time and accurate defect representation, while using the mesh of the entire unit cell yielded unreasonable computational resources. Hence, the original unit-cell mesh contained in the XCT STL file was reconditioned to represent only the selected strut (Fig. 2 (c, d)). The surface triangular grid was used to obtain the volumetric mesh, consisting of second-order - tetrahedral elements (C3D10, generated on Hypermesh) (Fig. 4 (a) and (b)).

The static structural analysis under quasi-static conditions was implemented to conduct a mechanical simulation using the commercial finite element (FE) software Ansys Workbench. All the models were subjected to the same boundary conditions reported in Fig. 4 (c). The bottom surface of the strut is constrained with zero displacement along the Y-axis and fixed rotations about the X, Y, and Z axes, while displacements along the X and Z axes remain free. On the top surface, a linear displacement is applied along the Y-axis, while rotations about all axes and displacements along the X and Z axes are fixed. In accordance with the strut centroid projections onto the top and bottom surfaces, two nodal lines were constrained in the z-direction to prevent rigid body rotation around the Y-axis (blue lines in Fig. 4 (c)).

To better detail the differences between the behaviour of the material, including (P model) or excluding the internal porosities (NP model), more specific analyses are carried out as follows. From the XCT reconstructed strut model, 250 equally spaced sections along the strut length and perpendicularly to the load direction were extracted. Each section is indexed with a number in ascending order, where section 0 corresponds to the surface on which displacement along the load direction is constrained equal to zero, while section 250 corresponds to the surface where the Y-displacement is applied. At each section, the surface area was measured (Fig. 4 (d)) for NP and P models. In Fig. 4 (d), the blue line refers to the NP model, which considers only external irregularities, while the red line refers to the P model, which includes the external irregularities and internal porosities and is called "pores". The corresponding dotted line indicated the average section calculated over of the entire strut. Obviously, the measured cross-sections of the P model are smaller or equal to the counterpart measured on the NP model.

For all simulations, the material model was implemented according to the Chaboche model of L-PBF/P PA2200 bulk tensile tests (Schob et al., 2019), which is based on an elastoplastic formulation. The Chaboche model is calibrated to accurately capture the onset of plastic deformation as reported in the literature, occurring just before global failure. This approach markedly differs from homogenised methods commonly used in the literature for failure modelling, such as the Gurson model (Bruson et al., 2023; Schob et al., 2019), where porosity is represented as an intrinsic material parameter, typically approximated by spherical voids. In those models, the effect of porosity is incorporated a priori into the constitutive behaviour, limiting their ability to investigate the specific mechanical response associated with realistic pore geometries and distributions (Schob et al., 2019). In contrast, the present work explicitly incorporates porosities reconstructed from XCT data, preserving their size, shape, and spatial position within the strut. This modelling strategy allows the analysis of localised stress and strain fields around irregular pores, which can lead to local yielding near critical defects, even while the global response of the strut remains nearly linear. By doing so, the model enables a more realistic prediction of potential sites for plastic deformation and damage initiation. The material parameters adopted in the simulation are as follows: Young's modulus E = 1450 MPa, Poisson's ratio μ = 0.4, and yield stress σ_F = 17.5 MPa. The nonlinear hardening behaviour is captured using two backstress components, with the following Chaboche parameters: C_1 = 7920.469 MPa, γ_1 = 387.81, C_2 = 600.026 MPa, and γ_2 = 63.986, as detailed in Ref (Schob et al., 2019).

To accurately capture the complex geometry of internal pores, a surface mesh size below 0.01 mm was adopted, as illustrated in Fig. 4 (a), (b) and (c). This level of refinement ensured high geometric fidelity and was validated through preliminary convergence studies, which confirmed the stability of peak stress values, particularly around small-radius defects. For the analysis of the single strut with a 2.5 mm length, Table 1 reports the number of nodes, elements and the relative computation time of the different strut models.

3. Results and discussion

3.1. In-situ tensile test and influence of defects

Fig. 5 a) shows the continuous loading of an ex-situ sample compared to the in-situ sample undergoing interrupted loading. The results and the curve agree with the data obtained by the experimental campaign in Ref. (Bruson et al., 2023). In addition, the comparison between these two samples indicates that the interrupted loading can produce a loading force–elongation curve similar to that recorded during the ex-situ loading. The final failure of the in-situ lattice was performed ex-situ, and the location of the final failure is shown in Fig. 3 b). No damage is observed in any of the imaged parts of the lattice until the XCT scanning at 600 N. As shown in Fig. 5 c), d), the damage produced between 500 N and 600 N localises in row iii of column 5 and column 2 (where the rupture is not fully completed), as well as in row iv of column 1.

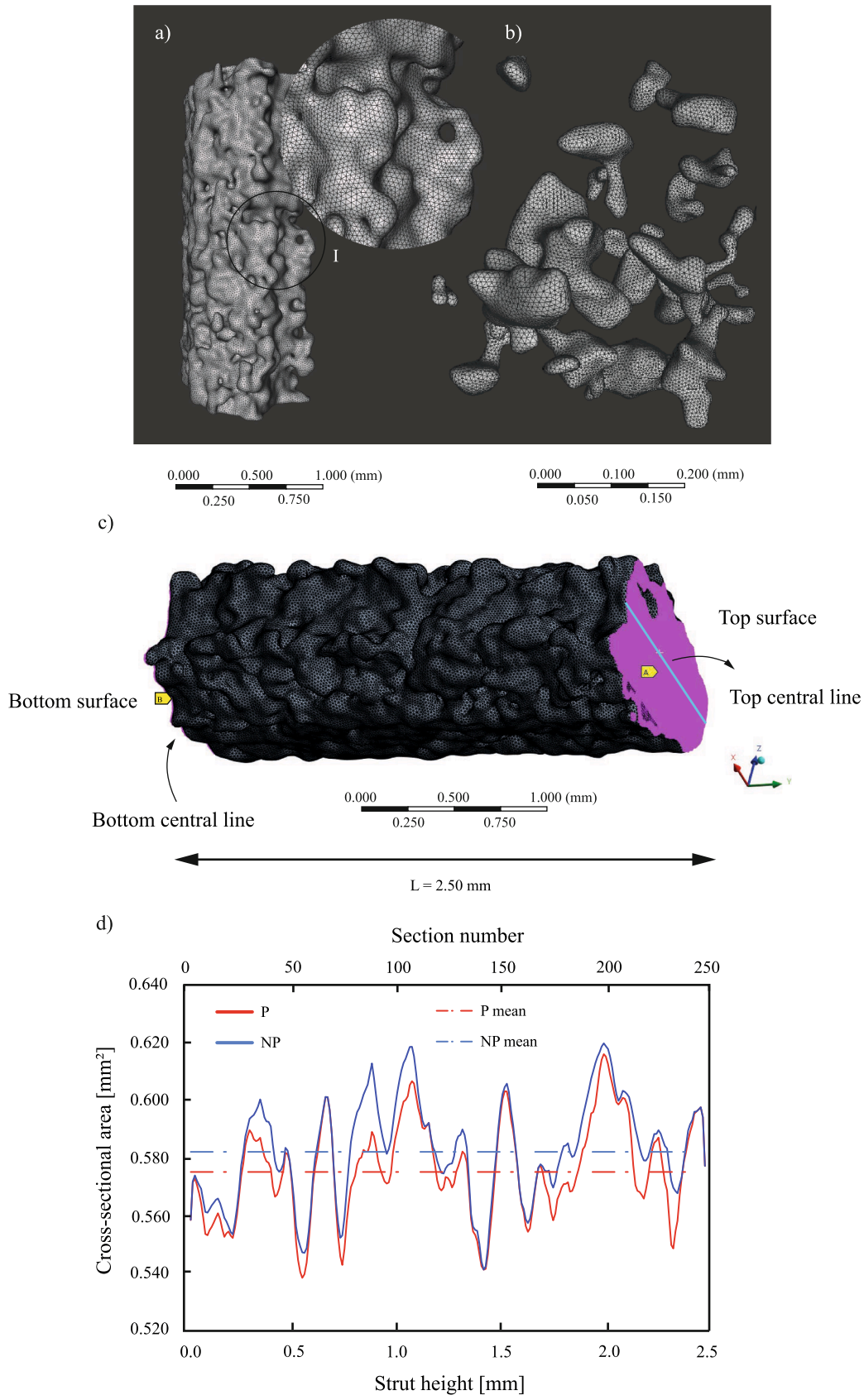

Fig. 4. a) Detail of the meshed surface roughness of the strut, b) detail of the meshed internal pores. c) Boundary conditions of the FE model using the XCT image-based mesh. d) Cross-sectional area distribution along the strut height for both the P and NP models.

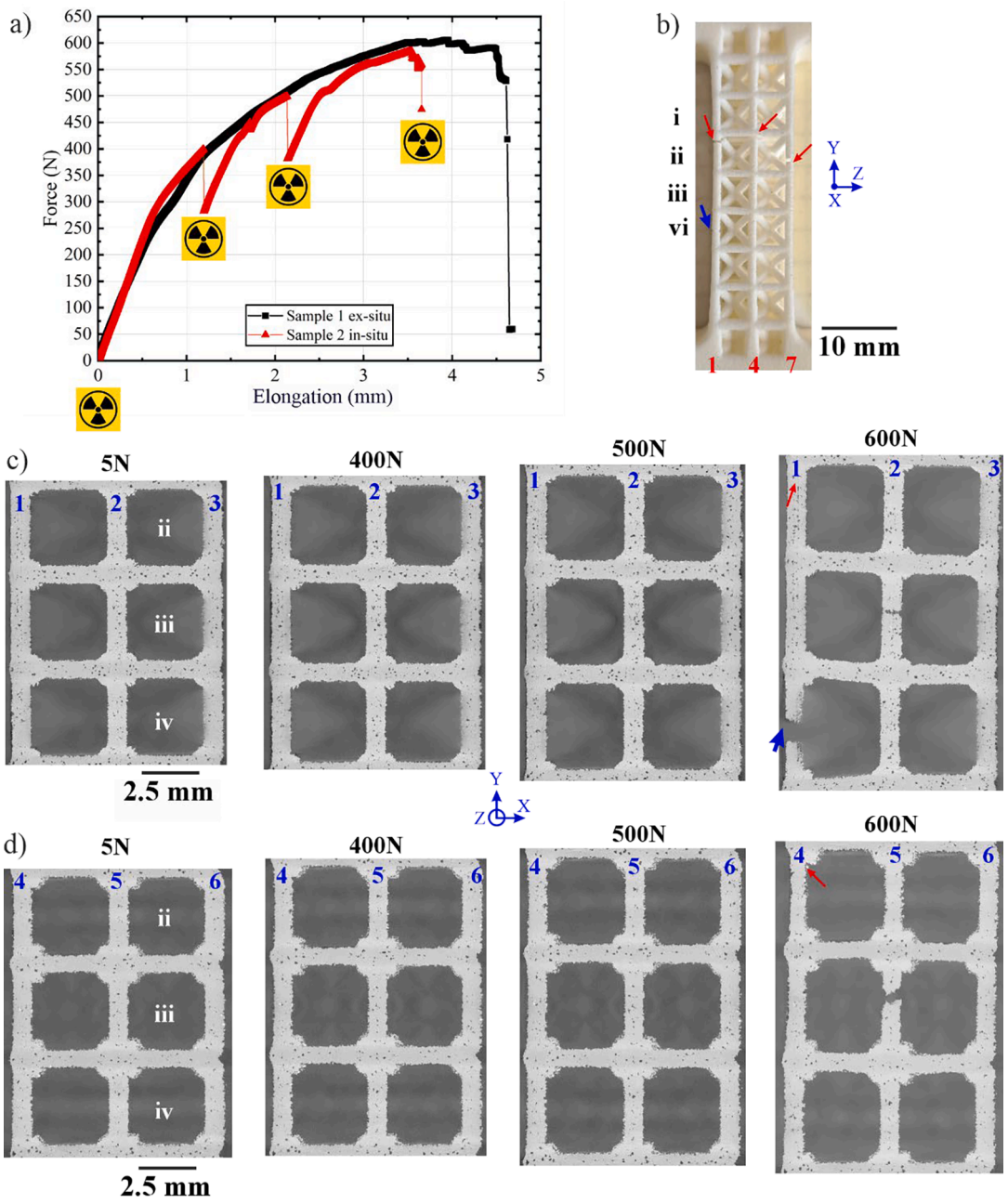

Fig. 5. a) Graph of the force against the elongation, indicating the steps where the loading was interrupted to perform xct scans. b) Image of the post-mortem sample: red arrows indicate the location of the final failure, from which the top and bottom part of the lattice are separated; the blue arrow indicates the occurrence of single strut breakage outside the fracture surface. c) Evolution of loading and damage for columns 1, 2, and 3. d) Evolution of loading and damaged for the columns 4, 5, and 6.

The literature has reported that imperfections inherited from the PBF-LB process govern the localisation of damage (e.g., (Sombatmai et al., 2021; Iantaffi et al., 2023; Sercombe et al., 2015). While the damage of process-induced porosities on mechanical properties has been widely studied at various levels (Sola and Nouri, 2019; Nicoletto et al., 2012; du Plessis et al., 2020), the role of intrinsic porosity in reticular structures fabricated via additive manufacturing remains less understood, particularly in terms of how the design and porosity distribution in the structure may influence strain and stress distributions and be potentially used as a functional feature. Therefore, a detailed characterisation of structural defects is shown in what follows. This characterisation focused on those defects contained within the vertical struts (i.e., those mainly carrying the tensile load) of the 5 N preloaded XCT dataset.

The volume fraction of the entire lattice is 1.6 % (Fig. 4 a)). In line with the literature (Iantaffi et al., 2023), the highest porosity level is observed at the nodes (3.0 % volume fraction), when compared to the vertical struts (i.e., those perpendicular to the BD, 1.2 %). The internal pores can be as large as 200 μm of EqD with Shape Factors up to about 14 (Fig. 6b) top). The majority of the pores have sizes between 30 μm and 100 μm and Shape Factors between 1 and 4. The combination of largest sizes and convoluted shapes can be the one that most influence the stress distribution because the sharp edges of elongated pores oriented perpendicular to the loading direction led to increased stress concentrations, when compared to those generated by spherical defects (Wang et al., 2019; Serrano-Munoz et al., 2018). Some of the internal pores with Shape Factors larger than 6 are shown in the bottom of Fig. 6 b)). These elongated pores tend to have their largest axis oriented parallel to

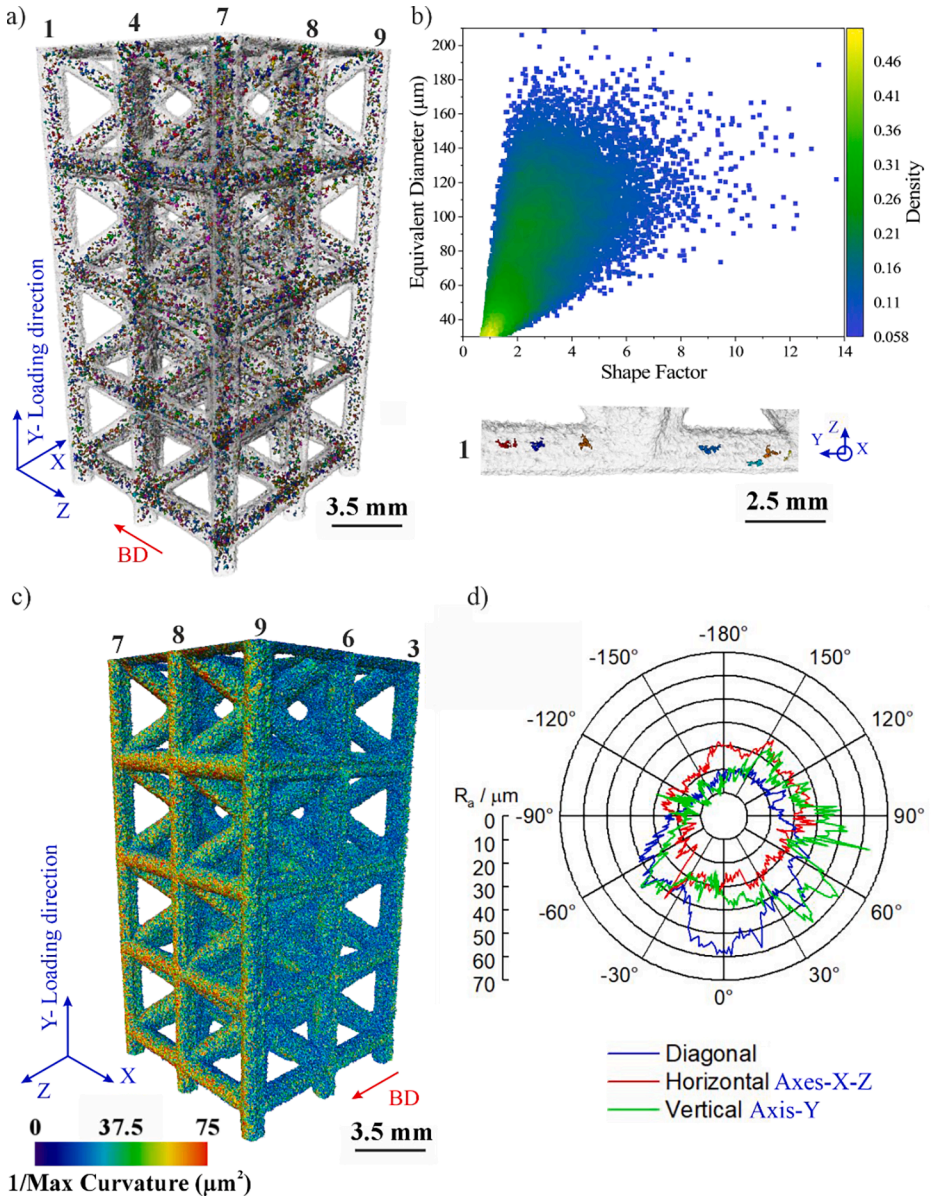

Fig. 6. a) 3D rendering of the internal pores contained in the imaged part of the lattice. b) density graph of the EqD against the shape factor at the top, and a 3D rendering of some pores larger than shape factor 6 contained within column 1 at the bottom. c) 3D rendering of the 1/max curvature computation. d) Polar graph of the Ra(θ), as calculated according to the procedure described in Section 2.2.2. The analysed struts are located at the centre of the lattice.

the loading direction.

Behind the internal pores, the surface topography of the strut and strut size are influenced by the heat exchange, peculiarity of the process. In terms of roughness, the main differences between upskin and downskin surfaces in PBF-LB/P, is that the upskin surface is located on top of layer solid material, while the downskin surface corresponds to the part of the strut surface that directly faces the powder bed (baseplate) without any supporting solid material. Therefore, the heat provided on top of an upskin surface could easily flow through the solid material, while the heat accumulates in a downskin surface because the powder, although sintered, is an insulating material. Therefore, as expected, the computation of the inverted maximum curvature (1/Max curvature) indicates that the surface roughness of the struts depends on the inclination angle and the orientation with respect to the build direction (BD) (Rack et al., 2008). The downskin of the struts exhibit the lowest surface roughness, or as shown in Fig. 6 c), the largest 1/Max curvature values. A detailed computation of the R_a parameter (i.e., the arithmetic average of the roughness profile) is shown in Fig. 6 d). As they are parallel to the BD, the horizontal strut shows the most homogenous roughness profile over the perimeter, with an R_a average of about 25 µm. On the other hand, the highest R_a values (about 60 µm) of the vertical and diagonal struts are located at the upskin (0°) and at 60°, respectively. This high value, comparable to the powder particles size, may be explained by the presence of residual sintered particles which strongly adhere to the part surfaces, and remain even after the cleaning process. As opposed to solid bulk samples, the cleaning procedure for complex reticular structures is considerably more complex due to the intricate reticular geometry and difficulty to individually access each strut in order to achieve a homogeneous cleaning (Calignano et al., 2022).

The thickness of the strut is influenced by the heat transfer. In fact, the thickness computation of the columns indicates a maximum variation of ± 50 µm and a minimum of 12 µm per strut (Fig. 7 a)), b)). Column 5 is, on average, the thickest one, whereas columns 1, 3, and 2 are the thinnest. As shown in the evaluation of the area fraction, these four columns also tend to concentrate the highest amounts of internal porosity (i.e., between 2 and 3 %), notably at the level of row iii (Fig. 7

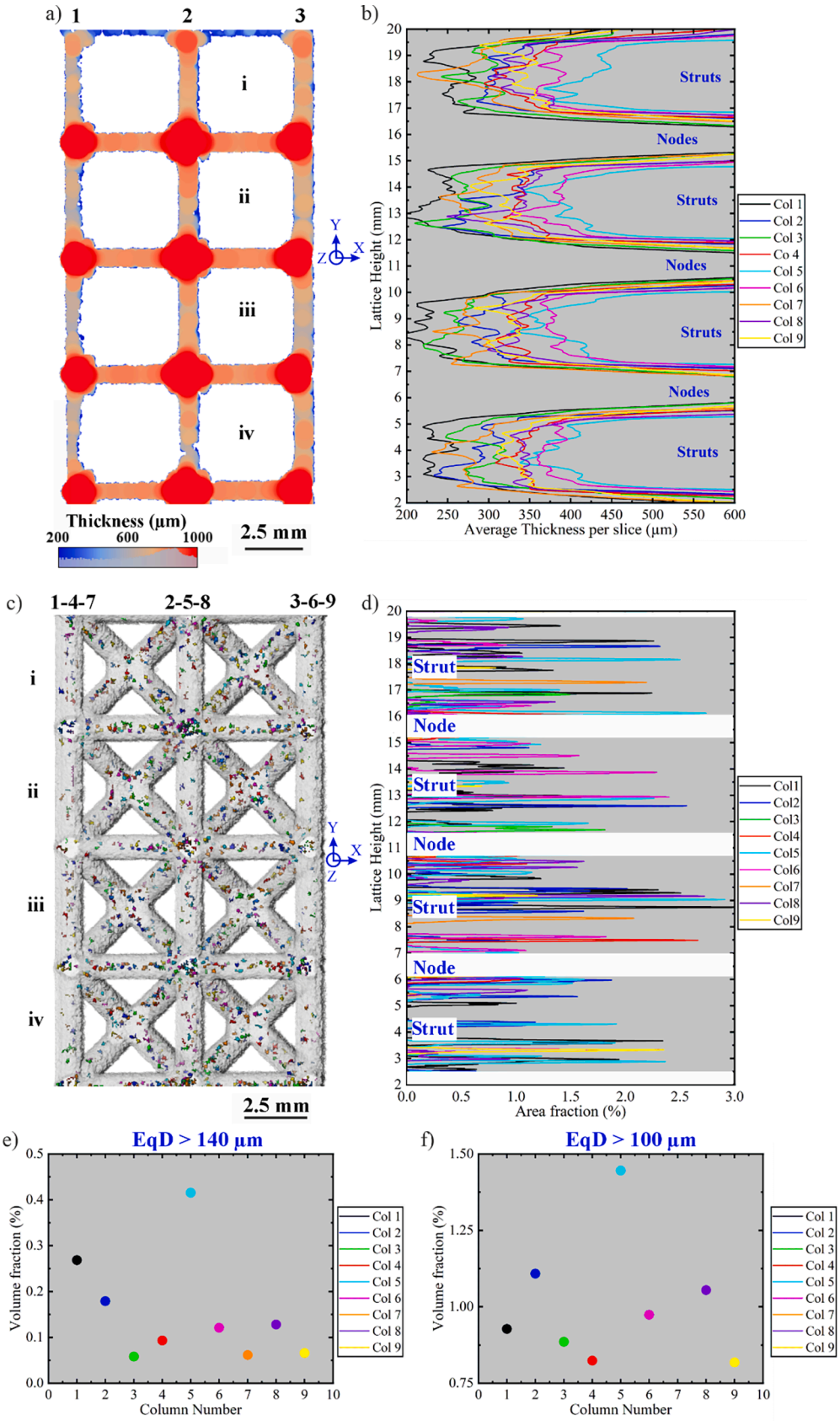

Fig. 7. a) Thickness map of a slice corresponding to columns 1, 2, and 3. for the sake of clarity, the computation is done without internal porosity. b) graph of the height of the lattice against the average thickness of the strut cross section per slice. c) 3D rendering of the pore population larger than EqD 140 μm, with d) corresponding graph of the height against the area fraction of internal porosity per slice. e) Graph of the volume fraction per column for the case of EqD > 140 μm, and f) for the case of EqD > 100 μm.

c), d)). This agrees with the fact that column 5 contains the largest volume fraction of internal porosity larger that EqD 140 μm, followed by columns 1 and 2 (Fig. 7 e)). Interestingly, the volume fraction of columns 1 and 2 evens out (i.e., falls in the 1.1 % to 0.8 % range) with the rest of the columns but column 5, when considering a porosity larger than 100 μm (Fig. 7 f)). This suggests that the large porosity controls the early damage instead of porosity clustering.

The failure site observed in row iii of column 5 (Fig. 5 d)) coincides with the highest (almost 3 %) amount of porosity occurring at the cross section, in combination with a reduced average thickness of 325 μm. However, this is not the case for column 1, which exhibits the combination of highest area fraction and lowest average thickness within row iii, and yet the failure site is observed to occur within row iv. The same situation applies to column 2, where the occurrence of failure does not coincide with the smallest cross section.

Further evaluation of the localisation of strain is performed by means of DVC between the steps at 400 and 500 N, where damage is not yet visually detected (Fig. 8). Again, this evaluation works well predicting the localisation of damage within row iii of column 5 (black arrow in Fig. 8 b)) but fails in the case of columns 1 and 2. Moreover, column 8 shows local values of strain that are higher than those observed in columns 1 and 2. Most probably the onset of failure occurs in column 5 and the load carrying capacity is unfavourably redistributed towards columns 1, 2 and 3, since they possess the lowest average thickness values. Note that columns 7, 8, and 9 are, in general, those exhibiting lower values of roughness. Hence, it could be also that a combination of reduced (from average) cross section with convoluted defects (e.g., small radii of curvature, which is not capture in the highest detail when using laboratory XCT) can in some cases be more critical to the strength than the smallest of cross sections per column alone.

3.2. Finite element analysis (FEA)

Fig. 9 compares the mechanical response regarding force–displacement up to a global strain equal to 1.25 % for the four models. As expected, the ideal CAD model exhibited the highest stiffness. Compared to the elliptic model, the predicted force reaction was 50 % higher. As can be observed, an elliptic model, which derives from the approximation of the process-induced geometrical error on the external shape of the strut (Bruson et al., 2023), can macroscopically well predict the force

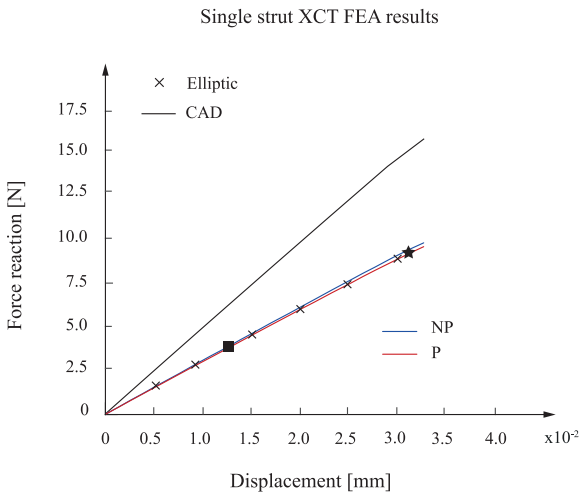

Fig. 9. Plot comparing the force–displacement FEA results between the nominal CAD, the elliptic cross-section approximation and the XCT reconstructions of the strut with (P) and without internal pores (NP). Square and star points correspond to a global strain level of 0.5% and 1.25%, respectively.

response compared to a higher level of modelling accuracy. From a macro point of view, therefore, the elliptical approximation compensated numerically for the process-induced external dimensional inaccuracies (deviation below 0.5 %). Thus, the presence of sintered particles on the surface could be described by considering a redistribution of the material. The elliptical section shows an area equal to 0.5091 mm^2, 35.2 % smaller than the CAD circular (equal to 0.7854 mm^2). Interestingly, the predicted reaction forces in the initial linear global response yielded only a marginal discrepancy between the elliptical model and the ones considering surface and surface plus internal defects. Consistent with the findings reported in the literature (Sombatmai et al., 2021), this observation suggests that the influence of porosities on the elastic and initial yielding responses is negligible. However, the presence of porosities controls the localisation of plastic strain, thus impacting the failure behaviour (Fig. 10). Therefore, homogenisation approaches for the material model as numerical hypotheses at the cell level are valid only under certain requirements (larger cell sizes to avoid

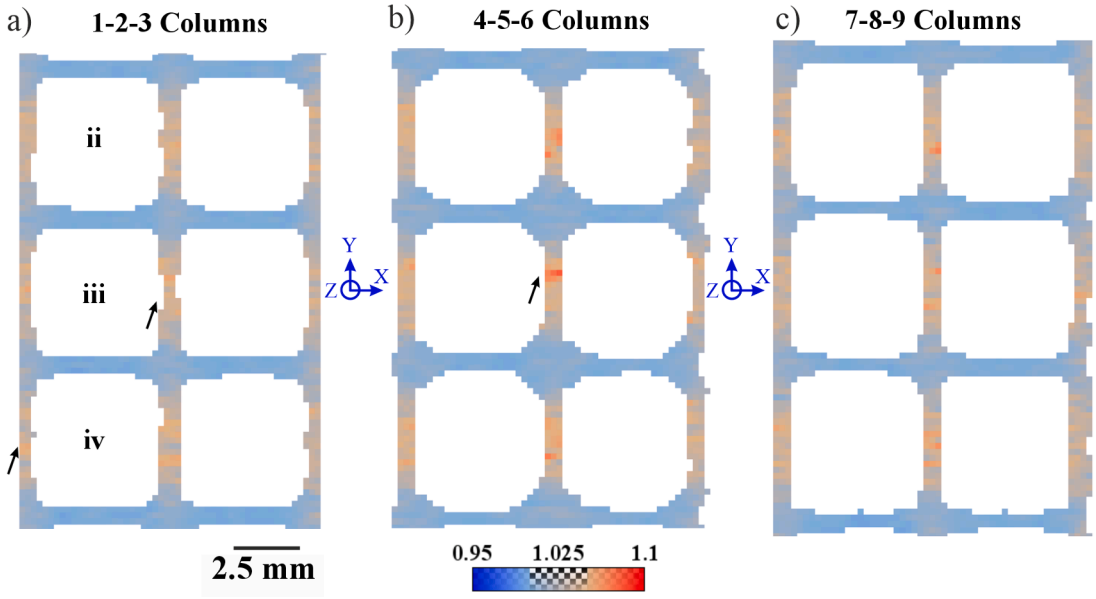

Fig. 8. DVD computation of the strain showing a slice corresponding to a) 1,2, and 3 columns; b) 4, 5, and 6 columns; and c) 7, 8, and 9 columns. The black arrows indicate the failure sites.

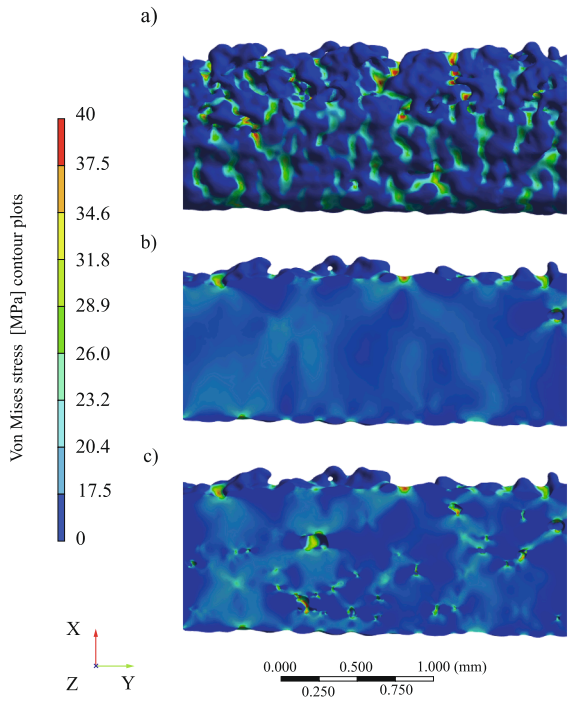

Fig. 10. Von Mises stress contour plots of a) XCT reconstructed strut surface, XCT reconstructed longitudinal mid-section of the strut at 1.25% global strain in b) NP model and c) P model.

size effect). For example, Fig. 10 shows the stress distribution at a global strain of 1.25 %. As can be observed, the convoluted surface of the strut, composed of partially sintered powder particles, and the presence of internal voids predominantly resulted in plastic localisation, in agreement with Ref. (Sombatmai et al., 2021). The uneven surface profile formed by the partially sintered powder particles led to an increase in local stress values as a consequence of the existence of numerous stress concentrators, which are generated by process-related surface imperfections of a microscopic scale surrounding the strut. These results explain the previously observed findings regarding the effect of the surface profile in developing a combined effect with internal pores, which collectively influence the failure mode by further localising the distribution of the stresses over the strut volume. Particularly, the simulated stress levels of powder particles that are loosely adhered to the surface of struts and partially sintered are exceedingly low, as illustrated in Fig. 10 (a), where these particles correspond to the surfaces rendered blue. The impact of these protruding particulates on the overall stress distribution is negligible. The porosity tends to be largest at the surface, corresponding to open pores and thus connected to the strut surface. This open porosity, as well as surface roughness valleys, are the main contributors to stress localisation (Fig. 10 (b)). Including internal porosity further increased the stress concentration, where stress bridges were induced between some of the open and internal porosity (Fig. 10 c)).

Specifically, Fig. 11 compares NP and P models at two intermediate global strain levels of the single strut: 0.5 % and 1.25 % (square and star in Fig. 9). In addition, the stress and the equivalent plastic strain (PEEQ) were analysed at each section of the strut (Fig. 4 (c)). A volume-weighted averaging procedure was implemented to determine the average stress and PEEQ values along each strut cross-section. Specifically, the average value over the cross-section was computed by performing a volume-weighted average of the element values. For each finite element intersecting the region encompassed by the cross-section, its contribution was calculated as the product of its individual value and corresponding volume. The total volume of all elements inside the section was then used to normalise the sum of the weighted contributions. This approach ensures that elements with larger volumes influence the average value proportionally more and vice versa, yielding a more physically representative measure of the local mechanical response.

At the selected strains, the volume of material in percentages exceeding local yielding stress values for P and NP models (assumed equal to 17.5 MPa) is 0.024 % at a global strain of 0.5 %. Therefore, the strain 0.5 % level is within the linear region of the global mechanical response of the structure (square in Fig. 9) and is used to evaluate the onset of stress concentration phenomena at the defects. On the other hand, at a global strain of 1.25 %, the P model displayed a 45.75 % volume yielded in the plastic region, while a higher 53.58 % was registered for the NP model. The strain 1.25 % is within the global initial plastic region (star in Fig. 9) and is used to identify the possible initiation points of damage. The first row in Fig. 11 (a), (c), (e) reports the result referring to a strain of 0.5 %, while the second row (b), (d), (f) refers to a strain of 1.25 %.

Overall, the trends between the two models are largely consistent and overlap substantially, meaning that peaks or valleys of stress or strain are observed around the same section in the two models.

As anticipated from the macroscopic observations (Fig. 9), the volume of material experiencing higher stress increases with the progression of global deformation (Fig. 11(a) and (b)). At equivalent strain levels, the majority of the material volume exhibits comparable stress values across the different models. However, the stress distribution within the material volume is narrower in the P model compared to the NP model. Specifically, the fraction of material subjected to lower stress values is lower in the P model relative to the NP model. The divergence between the two models becomes more pronounced at 1.25 % strain (Fig. 11(b)). This pattern is also reflected in the growing differences observed at the D10 and D90 percentiles of the cumulative stress distributions.

Observing Fig. 11 (c) and (d), overall, along the strut, the P model generally displays slightly lower average stress values across the entire strut. The most significant deviations between the models are observed in the sections of the strut between approximately 1 mm and 1.6 mm (Sections from 100 to 160). Evidently, the interaction between surface irregularities and internal porosities contributes the most to the stress redistribution in these areas.

In the NP model, the most stressed sections are near section 55 and, subsequently, section 75. However, in the P model, section 75 appeared more critically loaded than section 55. These sections are followed by the slightly inferior stress peaks localised near sections 141, 162, and 179, in which a significant difference can be observed between the two models. The region of the strut proximal to sections 141 and 162 shows peak intensities in the P model lower than the NP model, while the area around section 179 maintains a similar average stress level among the models. This result can be explained by observing the differences in cross-sectional area among the two models (Fig. 4 (c)). The highest average PEEQ values can be observed in the proximity of the same sections previously identified as critical (55, 75, 141, 162 and 179). However, for both models, at the first deformation stage (0.5 % global strain) (Fig. 11 (e)), plastic deformation is absent in most of the strut, and localised peaks are indicative of an initial stress concentration. At a strain equal to 1.25 % (Fig. 11 (f)), the differences among the two models became more significant, with strong evidence of localised deformation in the P model, in which, in certain sections, PEEQ values resulted in higher values than the corresponding NP section. Overall, the presence of internal pores can significantly change the stress distribution and consequently the stress values in the material.

For the sake of comparison, the four most critically stressed areas are compared. These areas can be localised near sections 23, 55, 75 and 179. Considering the presence of internal porosities, the cross-sectional areas can be ordered from smallest to largest as following: 75, 55, 23, and 179. Section 75 is the most critically stressed, followed by 55, 179, and 23. In agreement with the previous observations, and as shown in Fig. 12, surface-induced stress concentrations are most prominent in sections 55

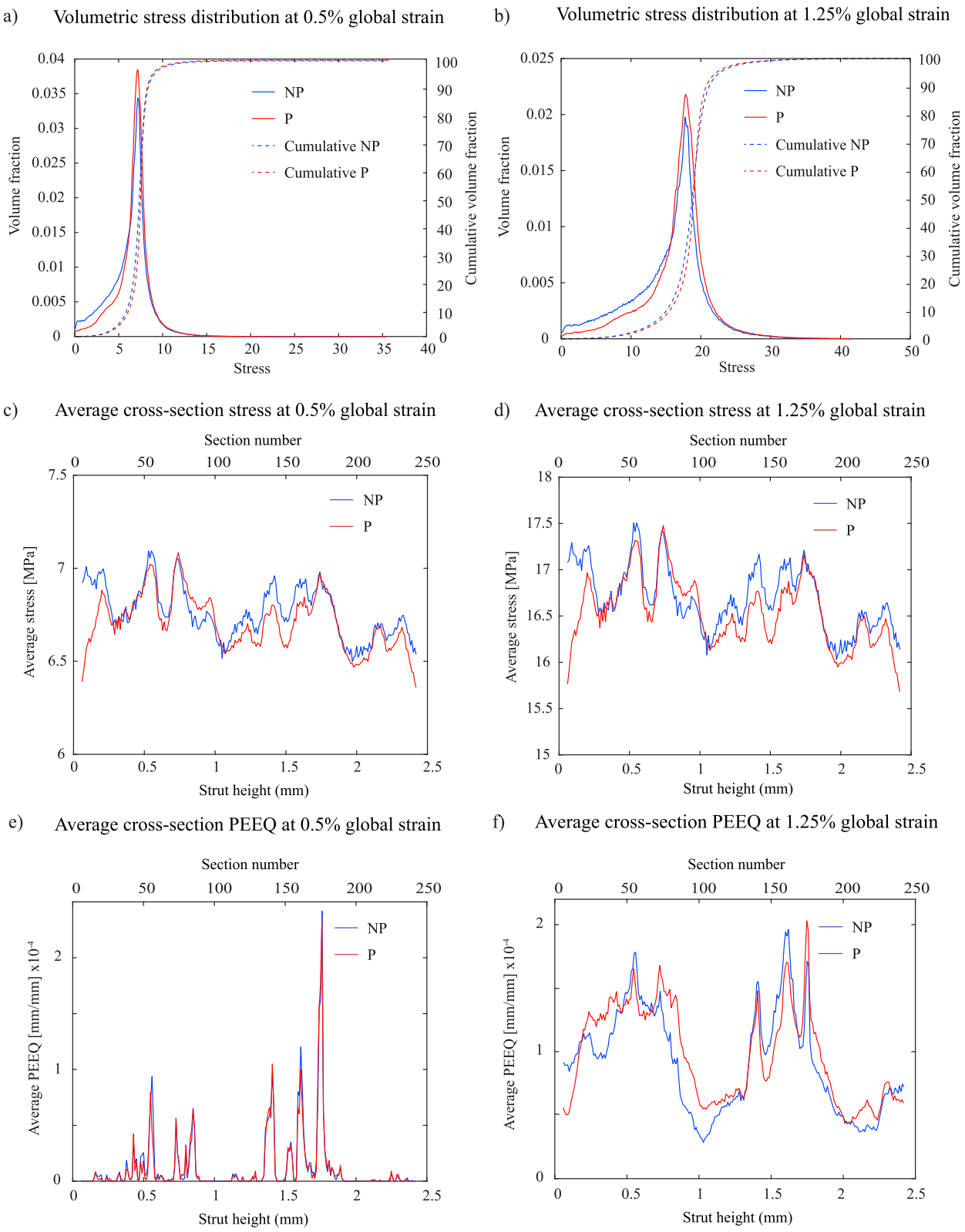

Fig. 11. Comparison between NP model (only external irregularities) in blue and P model in red (external irregularities and internal porosities) at 0.5% (a), (c), (e) and 1.25% (b), (d), (f) global strains in terms of: (a) and (b) global relative and cumulative stress distributions, (c) and (d) average stress along the strut, and (e) and (f) equivalent plastic strain (PEEQ) along the strut.

and 75, and considerably lower in sections 23 and 179.

In section 55, the average stress and PEEQ are lower when considering the internal pores. Near that section, an elongated open pore (Fig. 12 (a)) is located near the surface and appears to act as a stress concentrator. The P model contains three smaller, more circular pores than the one located on the surface. Those pores collectively redistribute the stresses (Fig. 12 (a) 55I) and contributes positively to the mechanical behaviour of the section by alleviating the localisation of stress

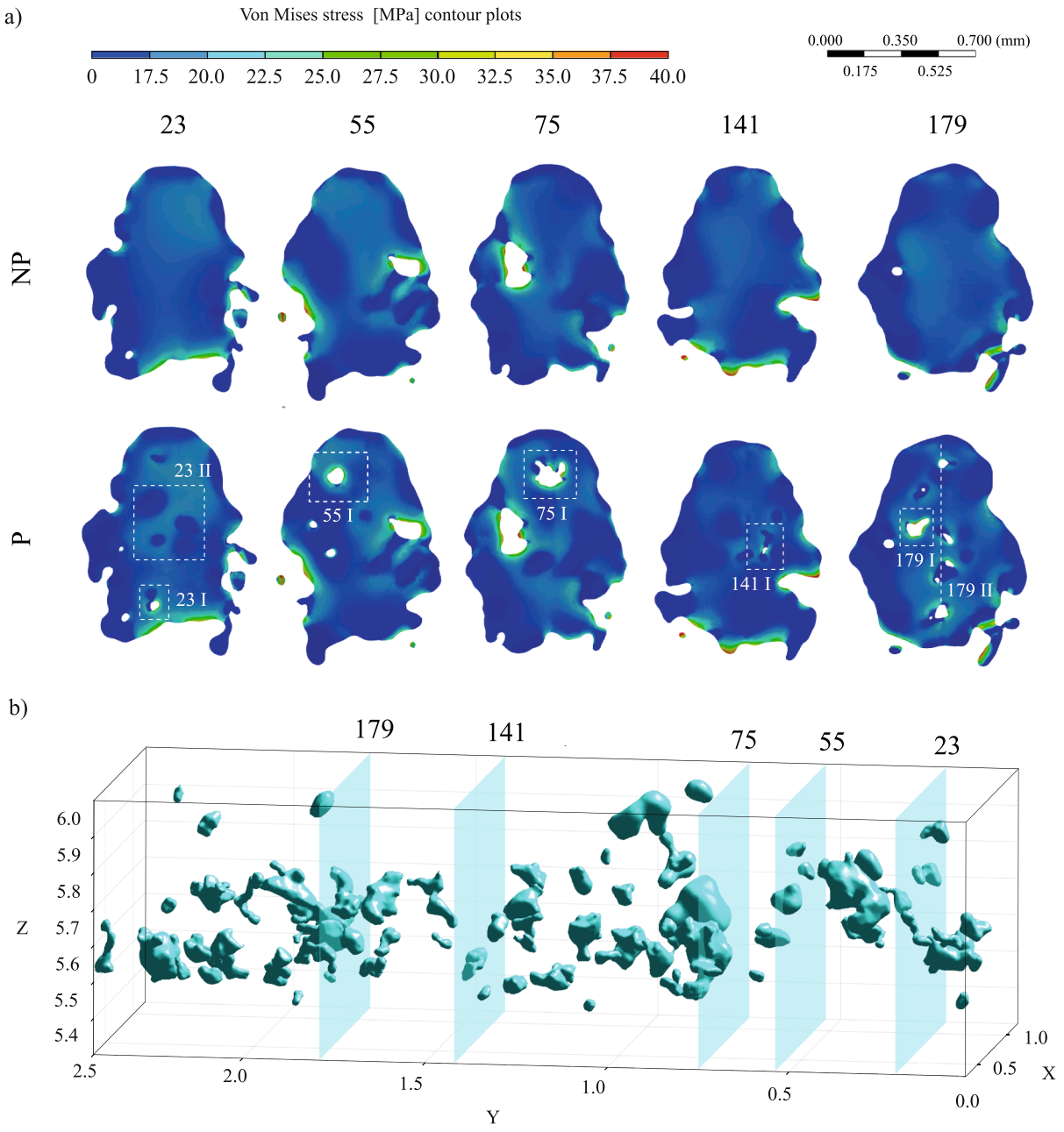

Fig. 12. (a) Detail of Von Mises contour plots at 1.25% global strain of the critical sections 23, 55, 75, 141 and 179 for the NP and P models and (b) a 3D visualization of their locations along the strut height in relation to internal porosities.

concentrations in critical zones In section 75, an open pore with irregular geometry (Fig. 12 (a) 75I), although less proximate to the surface respect to the one in section 55, acts as a site of severe local stress concentrations. P model presents an additional pore close to the surface, but slightly smaller with a highly irregular and jagged profile. In this case, both average stress and PEEQ are higher in the P model, indicating a detrimental effect of the internal porosity.

Section 23 features an extremely low porosity volume fraction (approximately 0.225 %). The single elongated pore near the surface induces a local peak in stress (as shown in Fig. 12 (a) 23I). However, the stress redistribution provided by surrounding pores in the near sections (Fig. 12 (b) 23 II) reduces the mean cross-sectional stress, thereby mitigating the impact of the surface-near defect. Indeed, while surface PEEQ is lower in the P model, localised plastic deformation is concentrated around the pore boundaries (see Fig. 12 (a) 23i), consistent with stress concentration behaviour.

In Section 179, there is no significant modification of stresses among the two models, whereas PEEQ increases markedly throughout deformation (Fig. 11 (c) vs (d)). The internal pores are irregular and sharp (Fig. 12 (a) 179II). It can be observed that the most acute corner of the pore, highlighted in the section (Fig. 12 (a) 179I), is the site of the highest local stress concentration. Compared to section 75, which features a pore of similar geometry, the presence of additional pores in section 179 appears to partially mitigate the detrimental effect, similar to what was observed in Section 23. Therefore, despite having a larger cross-sectional area and lower surface-related stress effects, section 179 still shows high average stress values, suggesting that smaller, highly irregular pores may be more detrimental than previously assumed,

sometimes even more than the cross-sectional area alone would predict. This observation is in line with experimental in-situ testing results, and it supports the hypothesis that a combination of reduced local cross-section and complex pore morphology (e.g., sharp corners or small radii of curvature not fully resolved by laboratory XCT) can pose a greater threat to mechanical integrity than simple geometric thinning. Therefore, the most critical section in the strut appears to be defined by a combined interplay of surface effects, local cross-sectional reduction, and the size, shape, and position of internal porosity.

To better understand the possible initiation damage sites in the strut, the local elastic modulus (E_{local}) has been calculated at each section within the global linear response of the strut as reported in Equation (1):

$$E_{local} = \frac{\sigma_2 - \sigma_1}{\varepsilon_2 - \varepsilon_1} \quad (1)$$

where σ_1 and σ_2 and $\varepsilon_1$and ε_2 are the numerical normal average cross-section stresses and strains at 0.25 % and 0.5 % of the initial linear global deformation of the strut. The result of the local elastic modulus values along the strut at each section is reported in Fig. 13. As it can be observed, the values oscillate around the nominal modulus of the base material model (black line in Fig. 13). Where the cross-sectional area results smaller than the average (Fig. 4 (c)), the local elastic modulus is higher than that of the bulk material, whereas larger cross-sections exhibit lower modulus values. This behaviour reflects the influence of geometric defects on stiffness and is consistent with previous observations.

The presence of internal porosity generally mitigates both the fluctuations in elastic modulus and the stress concentrations caused by external surface irregularities (Fig. 13). The peak of the local elastic modulus is located near section 141. This section is one of the smallest cross-sectional areas along the strut and exhibits a lower average stress compared to the more critically stressed sections (55 and 75). In such a section, the presence of pores again significantly decreases the average stress with respect to those detected in the NP model. As shown in Fig. 12 (a) 141 I, a single small, circular pore is adjacent to a surface notch. This pore undergoes high local deformation and contributes to stress redistribution, leading to a lower sectional average stress. Nonetheless, its limited size relative to the stressed surface area restricts its ability to plastically accommodate the load. The coexistence of a minimal cross-section and a pronounced surface stress concentration

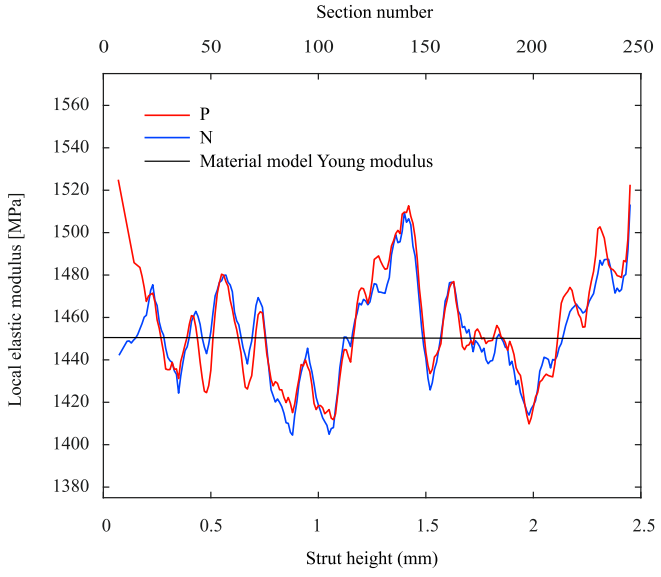

Fig. 13. Local elastic modulus calculated per section for the P (red) and NP (blue) models. The black line represents the Young's modulus used in the material model assigned to the uniform bulk material.

significantly limits the deformation capacity of this section. This effect results in a maximum local elastic modulus, potentially indicating a brittle fracture onset at the surface notch. The presence of a single internal pore, at least within the globally linear elastic regime, may partially mitigate this brittleness by reducing the gap between the local stiffness and the nominal bulk modulus.

In contrast, section 75 registers the highest deformations, associated with a high average stress and a local elastic modulus close to the Young's modulus of the material. This section accommodates the majority of the global deformation, favouring a ductile failure mechanism initiating at the pore sites (higher stress in the surfaces in Fig. 12 (a) 75 I). Despite the pore mitigation effect and a slightly bigger cross-section area, section 141 may still fail earlier under lower applied stress levels due to the local stiffness peak induced by the sharp surface notch. Analogous considerations can be made about the other local elastic modulus peaks in Fig. 13.

4. Conclusion

Reticular structures are fascinating for many applications. Despite being attractive for many reasons, such as their light weight, these thin structures appear inadequate in mechanical applications. This feeling may be generated by the scarce knowledge and deep characterisation of the failure modes. This work characterised the role of external irregularities and internal porosity on the mechanical response of lattices produced by PBF-LB/P. In situ laboratory X-ray computed tomography was performed using one of the most known lattice structures: the BCC. Numerical simulations were implemented and resolved using FEM for the further elucidation of the experimental observation. The samples were produced by PBF-LB/P in PA2200, which is typically affected by natural internal porosities due to the sintering process. The main conclusions can be drawn as follows:

1. The structure exhibited an average porosity of 1.6 %, with pores concentrated in the nodes (up to 3 %) and vertical struts (1.2 %). Elongated pores aligned with the load direction, especially in column 5, combined with local thinning, were found to be the most detrimental.
2. DVC analysis revealed early strain localisation in column 5 at 500 N, consistent with experimental failure. However, failure in columns 1 and 2 was less clearly anticipated by DVC, indicating a more complex interplay of defects beyond strain accumulation alone.
3. In the experimental in situ testing, damage was first observed between 500–600 N and localised in columns 1, 2, and 5. The final fracture occurred in the same area, confirming early damage accumulation in specific columns of the sample.
4. Simulations showed that a simple elliptical approximation of the strut cross-section, accounting for external geometric deviations, produced a force–displacement response within 0.5 % of more complex models that included actual surface and internal defects. The elliptical model, with 35.2 % less cross-sectional area than the nominal CAD, provides a computationally efficient alternative for global stiffness prediction.
5. The numerical analyses revealed that including internal porosity significantly increased localised stress and equivalent plastic strain, reducing the average stress per section. At 1.25 % global strain, the model in which only the surface irregularities are included showed that 53.58 % of the material exceeds the yield stress. This percentage drops to 45.75 % when simulating the surface irregularities and the internal model.
6. From the numerical outcome, it was possible to identify the section with the highest average stresses and PEEQ values. In those sections, it was possible to observe that even a single irregular pore can induce stress amplification, while smaller, more circular pores facilitated stress redistribution. The section that showed the minimal porosity also showed a reduced average stress, displayed high stiffness and

severe surface notch effects, suggesting a potential initiation site of brittle failure under lower stress.
7. The numerical analysis showed that the local elastic modulus is higher in sections with reduced cross-sectional area. Internal porosity tended to mitigate surface-induced stress peaks, smoothing local stiffness variations.

Overall, internal porosity attenuates both the amplitude of elastic modulus fluctuations and the severity of stress concentrations induced by surface irregularities, acting at the microstructural level, as natural strain/stress concentrators. While this behaviour is typically considered detrimental, the results support a possible emerging concept of defect-aware design, where even inherently defective features as porosity might be strategically arranged to control deformation and promote predictable, non-catastrophic failure. These findings demonstrate that failure in thin-walled additive-manufactured lattice structures cannot be predicted solely by minimum cross-section or porosity fraction. Instead, a combined influence of cross-sectional reduction, pore morphology, location, and surface roughness oversees the onset of plastic deformation and failure. High-fidelity models, including XCT-based reconstructions of real defects, are essential to capture this interplay.

Funding sources

This research received no specific grant from funding agencies in the public, commercial, or not-for-profit sectors.

CRediT authorship contribution statement

Danilo Bruson: Writing – review & editing, Writing – original draft, Visualization, Methodology, Investigation, Formal analysis, Data curation, Conceptualization. **Itziar Serrano-Munoz:** Writing – original draft, Visualization, Resources, Methodology, Investigation, Formal analysis, Data curation. **Tobias Fritsch:** Writing – original draft, Visualization, Methodology. **Henning Markötter:** Writing – original draft, Methodology, Data curation. **Manuela Galati:** Writing – review & editing, Supervision, Resources, Methodology, Investigation, Conceptualization.

Declaration of competing interest

The authors declare that they have no known competing financial interests or personal relationships that could have appeared to influence the work reported in this paper.

Acknowledgements

The authors thank Bundesanstalt für Materialforschung und -prüfung (BAM) for hosting and supporting Amir Zayergolhin during his internship. His assistance and collaboration during the in-situ tests are highly appreciated.

Data availability

Data will be made available on request.

References

Bai, L., Gong, C., Chen, X., Sun, Y., Xin, L., Pu, H., Peng, Y., Luo, J., 2020. Mechanical properties and energy absorption capabilities of functionally graded lattice structures: Experiments and simulations. Int. J. Mech. Sci. https://doi.org/10.1016/j.ijmecsci.2020.105735.

Bruson, D., Galati, M., Calignano, F., Iuliano, L., 2023. Mechanical characterisation and simulation of the tensile behaviour of polymeric additively manufactured lattice structures. Exp. Mech. 63. https://doi.org/10.1007/s11340-023-00976-5.

Buades, A., Coll, B., Morel, J.-M., 2011. Non-local means denoising. Image Processing on Line 1. https://doi.org/10.5201/ipol.2011.bcm_nlm.

Calignano, F., Giuffrida, F., Galati, M., 2021. Effect of the build orientation on the mechanical performance of polymeric parts produced by multi jet fusion and selective laser sintering. J. Manuf. Process. https://doi.org/10.1016/j.jmapro.2021.03.018.

Calignano, F., Mercurio, V., Rizza, G., Galati, M., 2022. Investigation of surface shot blasting of AlSi10Mg and Ti6Al4V components produced by powder bed fusion technologies. Precis. Eng. 78. https://doi.org/10.1016/j.precisioneng.2022.07.008.

Červinek, O., Werner, B., Koutný, D., Vaverka, O., Pantělejev, L., Paloušek, D., 2021. Computational approaches of quasi-static compression loading of SS316L lattice structures made by selective laser melting. Materials 14. https://doi.org/10.3390/ma14092462.

Dressler, A.D., Jost, E.W., Miers, J.C., Moore, D.G., Seepersad, C.C., Boyce, B.L., 2019. Heterogeneities dominate mechanical performance of additively manufactured metal lattice struts. Addit. Manuf. 28. https://doi.org/10.1016/j.addma.2019.06.011.

du Plessis, A., Yadroitsava, I., Yadroitsev, I., 2020. Effects of defects on mechanical properties in metal additive manufacturing: a review focusing on X-ray tomography insights. Mater. Des. 187. https://doi.org/10.1016/j.matdes.2019.108385.

Feldkamp, L.A., Davis, L.C., Kress, J.W., 1984. Practical cone-beam algorithm. J. Opt. Soc. Am. A 1. https://doi.org/10.1364/josaa.1.000612.

Fritsch, T., Farahbod-Sternahl, L., Serrano-Muñoz, I., Léonard, F., Haberland, C., Bruno, G., 2022. 3D computed tomography quantifies the dependence of bulk porosity, surface roughness, and re-entrant features on build angle in additively manufactured IN625 lattice struts. Adv. Eng. Mater. 24. https://doi.org/10.1002/adem.202100689.

Giannitelli, S.M., Accoto, D., Trombetta, M., Rainer, A., 2014. Current trends in the design of scaffolds for computer-aided tissue engineering. Acta Biomater. 10, 580–594. https://doi.org/10.1016/J.ACTBIO.2013.10.024.

González-Henríquez, C.M., Sarabia-Vallejos, M.A., Rodriguez-Hernandez, J., 2019. Polymers for additive manufacturing and 4D-printing: materials, methodologies, and biomedical applications. Prog. Polym. Sci. 94, 57–116. https://doi.org/10.1016/J.PROGPOLYMSCI.2019.03.001.

Gümrük, R., Mines, R.A.W., 2013. Compressive behaviour of stainless steel micro-lattice structures. Int. J. Mech. Sci. 68, 125–139. https://doi.org/10.1016/J.IJMECSCI.2013.01.006.

Gürsoy, D., De Carlo, F., Xiao, X., Jacobsen, C., 2014. TomoPy: a framework for the analysis of synchrotron tomographic data. J. Synchrotron Radiat. 21. https://doi.org/10.1107/S1600577514013939.

Han, W., Kong, L., Xu, M., 2022. Advances in selective laser sintering of polymers. Int. J. Extreme Manuf. 4. https://doi.org/10.1088/2631-7990/ac9096.

Hildebrand, T., Rüegsegger, P., 1997. A new method for the model-independent assessment of thickness in three-dimensional images. J. Microsc. 185. https://doi.org/10.1046/j.1365-2818.1997.1340694.x.

Iantaffi, C., Bele, E., McArthur, D., Lee, P.D., Leung, C.L.A., 2023. Auxetic response of additive manufactured cubic chiral lattices at large plastic strains. Mater. Des. 233. https://doi.org/10.1016/j.matdes.2023.112207.

Leary, M., Mazur, M., Elambasseril, J., McMillan, M., Chirent, T., Sun, Y., Qian, M., Easton, M., Brandt, M., 2016. Selective laser melting (SLM) of AlSi12Mg lattice structures. Mater. Des. 98, 344–357. https://doi.org/10.1016/J.MATDES.2016.02.127.

Lei, H., Li, C., Meng, J., Zhou, H., Liu, Y., Zhang, X., Wang, P., Fang, D., 2019. Evaluation of compressive properties of SLM-fabricated multi-layer lattice structures by experimental test and μ-CT-based finite element analysis. Mater. Des. 169, 107685. https://doi.org/10.1016/J.MATDES.2019.107685.

Li, P.Y., Sun, W.B., Zhang, W., Ma, Y.E., 2024. Effect of geometric defects on the mechanical properties of additive manufactured Ti6Al4V lattice structures. Thin-Walled Struct. 205, 112497. https://doi.org/10.1016/J.TWS.2024.112497.

Liebrich, A., Langowski, H.C., Schreiber, R., Pinzer, B.R., 2019. Porosity distribution in laser-sintered polymeric thin sheets as revealed by X-ray micro tomography. Polym Test 76. https://doi.org/10.1016/j.polymertesting.2019.02.014.

Lindberg, A., Alfthan, J., Pettersson, H., Flodberg, G., Yang, L., 2018. Mechanical performance of polymer powder bed fused objects – FEM simulation and verification. Addit. Manuf. https://doi.org/10.1016/j.addma.2018.10.009.

Lozanovski, B., Downing, D., Tino, R., du Plessis, A., Tran, P., Jakeman, J., Shidid, D., Emmelmann, C., Qian, M., Choong, P., Brandt, M., Leary, M., 2020. Non-destructive simulation of node defects in additively manufactured lattice structures. Addit Manuf 36. https://doi.org/10.1016/j.addma.2020.101593.

Markötter, H., Sintschuk, M., Britzke, R., Dayani, S., Bruno, G., Bhattacharyya, D., 2022. Upgraded imaging capabilities at the BAMline (BESSY II). J. Synchrotron Radiat. 29. https://doi.org/10.1107/S1600577522007342.

Markötter, H., Müller, B.R., Kupsch, A., Evsevleev, S., Arlt, T., Ulbricht, A., Dayani, S., Bruno, G., 2023. A review of X-ray imaging at the BAMline (BESSY II). Adv. Eng. Mater. 25. https://doi.org/10.1002/adem.202201034.

Marschall, D., Rippl, H., Ehrhart, F., Schagerl, M., 2020. Boundary conformal design of laser sintered sandwich cores and simulation of graded lattice cells using a forward homogenization approach. Mater. Des. 190. https://doi.org/10.1016/j.matdes.2020.108539.

Maskery, I., Aremu, A.O., Simonelli, M., Tuck, C., Wildman, R.D., Ashcroft, I.A., Hague, R.J.M., 2015. Mechanical properties of ti-6Al-4V selectively laser melted parts with body-centred-cubic lattices of varying cell size. Exp. Mech. https://doi.org/10.1007/s11340-015-0021-5.

Mazur, M., Leary, M., McMillan, M., Sun, S., Shidid, D., Brandt, M., 2017. Mechanical properties of Ti6Al4V and AlSi12Mg lattice structures manufactured by selective laser melting (SLM). Laser Additive Manufacturing: Materials, Design, Technologies, and Applications 119–161. https://doi.org/10.1016/B978-0-08-100433-3.00005-1.

Molavitabrizi, D., Bengtsson, R., Botero, C., Rännar, L.E., Mahmoud Mousavi, S., 2022. Damage-induced failure analysis of additively manufactured lattice materials under uniaxial and multiaxial tension. Int. J. Solids Struct. 252. https://doi.org/10.1016/j.ijsolstr.2022.111783.

della Ventura, N.M., Dong, C.Q., Messina, S.A., Collino, R.R., Balbus, G.H., Donegan, S. P., Miller, J.D., Gianola, D.S., Begley, M.R., 2024. Heterogeneity in millimeter-scale Ti-6Al-4V lattice primitives: Challenges in defining effective properties for metamaterial design, Mater Des 238, https://doi.org/10.1016/j.matdes.2024.112695.

Nicoletto, G., Konečná, R., Fintova, S., 2012. Characterization of microshrinkage casting defects of al-si alloys by X-ray computed tomography and metallography. Int. J. Fatigue. https://doi.org/10.1016/j.ijfatigue.2012.01.006.

Otsu, N., 1979. Threshold selection method from gray-level histograms. IEEE Trans. Syst. Man Cybern. SMC-9. https://doi.org/10.1109/tsmc.1979.4310076.

Păcurar, R., Berce, P., Petrilak, A., Nemeş, O., Miron Borzan, C.Ş., Harničárová, M., Păcurar, A., 2021. Selective laser sintering of PA 2200 for hip implant applications: finite element analysis, process optimization, morphological and mechanical characterization. Materials 14. https://doi.org/10.3390/ma14154240.

Pan, C., Han, Y., Lu, J., n.d. Design and Optimization of Lattice Structures: A Review, https://doi.org/10.3390/app10186374.

Pavan, M., Craeghs, T., Verhelst, R., Ducatteeuw, O., Kruth, J.P., Dewulf, W., 2016. CT-based quality control of laser sintering of polymers. Case Studies in Nondestructive Testing and Evaluation 6. https://doi.org/10.1016/j.csndt.2016.04.004.

Porter, D.A., Di Prima, M.A., Badhe, Y., Parikh, A.R., 2022. Nylon lattice design parameter effects on additively manufactured structural performance. J. Mech. Behav. Biomed. Mater. https://doi.org/10.1016/j.jmbbm.2021.104869.

Rack, A., Zabler, S., Müller, B.R., Riesemeier, H., Weidemann, G., Lange, A., Goebbels, J., Hentschel, M., Görner, W., 2008. High resolution synchrotron-based radiography and tomography using hard X-rays at the BAMline (BESSY II). Nucl. Instrum. Methods Phys. Res. A 586. https://doi.org/10.1016/j.nima.2007.11.020.

Schindelin, J., Arganda-Carreras, I., Frise, E., Kaynig, V., Longair, M., Pietzsch, T., Preibisch, S., Rueden, C., Saalfeld, S., Schmid, B., Tinevez, J.Y., White, D.J., Hartenstein, V., Eliceiri, K., Tomancak, P., Cardona, A., 2012. Fiji: an open-source platform for biological-image analysis. Nat. Methods 9. https://doi.org/10.1038/nmeth.2019.

Schmid, M., 2018. Laser Sintering with Plastics. https://doi.org/10.3139/9781569906842.

Schob, D., Roszak, R., Sagradov, I., Sparr, H., Ziegenhorn, M., Kupsch, A., Léonard, F., Müller, B.R., Bruno, G., 2019. Experimental determination and numerical simulation of material and damage behaviour of 3D printed polyamide 12 under quasi-static loading. Arch. Mech. 71. https://doi.org/10.24423/aom.3162.

Sercombe, T.B., Xu, X., Challis, V.J., Green, R., Yue, S., Zhang, Z., Lee, P.D., 2015. Failure modes in high strength and stiffness to weight scaffolds produced by selective laser melting. Mater. Des. 67. https://doi.org/10.1016/j.matdes.2014.10.063.

Serrano-Munoz, I., Buffiere, J.Y., Verdu, C., 2018. Casting defects in structural components: are they all dangerous? a 3D study. Int. J. Fatigue 117. https://doi.org/10.1016/j.ijfatigue.2018.08.019.

Sindinger, S.L., Kralovec, C., Tasch, D., Schagerl, M., 2020. Thickness dependent anisotropy of mechanical properties and inhomogeneous porosity characteristics in laser-sintered polyamide 12 specimens. Addit. Manuf. 33. https://doi.org/10.1016/j.addma.2020.101141.

Sindinger, S.L., Marschall, D., Kralovec, C., Schagerl, M., 2021. Material modelling and property mapping for structural FEA of thin-walled additively manufactured components. Virtual Phys. Prototyp. 16. https://doi.org/10.1080/17452759.2020.1824427.

Sola, A., Nouri, A., 2019. Microstructural porosity in additive manufacturing: the formation and detection of pores in metal parts fabricated by powder bed fusion. J. Adv. Manuf. Process 1. https://doi.org/10.1002/amp2.10021.

Sombatmai, A., Uthaisangsuk, V., Wongwises, S., Promoppatum, P., 2021. Multiscale investigation of the influence of geometrical imperfections, porosity, and size-dependent features on mechanical behavior of additively manufactured Ti-6Al-4V lattice struts. Mater. Des. 209, 109985. https://doi.org/10.1016/J.MATDES.2021.109985.

Somlo, K., Chauhan, S.S., Niordson, C.F., Poulios, K., 2022. Uniaxial tensile behaviour of additively manufactured elastically isotropic truss lattices made of 316L. Int. J. Solids Struct. 246–247. https://doi.org/10.1016/j.ijsolstr.2022.111599.

Stamati, O., Andò, E., Roubin, E., Cailletaud, R., Wiebicke, M., Pinzon, G., Couture, C., Hurley, R., Caulk, R., Caillerie, D., Matsushima, T., Bésuelle, P., Bertoni, F., Arnaud, T., Laborin, A., Rorato, R., Sun, Y., Tengattini, A., Okubadejo, O., Colliat, J.-B., Saadatfar, M., Garcia, F., Papazoglou, C., Vego, I., Brisard, S., Dijkstra, J., Birmpilis, G., 2020. spam: software for practical analysis of materials. J. Open Source Softw. 5. https://doi.org/10.21105/joss.02286.

Suard, M., Martin, G., Lhuissier, P., Dendievel, R., Vignat, F., Blandin, J.J., Villeneuve, F., 2015. Mechanical equivalent diameter of single struts for the stiffness prediction of lattice structures produced by electron beam melting. Addit. Manuf. 8. https://doi.org/10.1016/j.addma.2015.10.002.

Tan, L.J., Zhu, W., Zhou, K., 2020. Recent progress on polymer materials for additive manufacturing. Adv. Funct. Mater. https://doi.org/10.1002/adfm.202003062.

Tasch, D., Mad, A., Stadlbauer, R., Schagerl, M., 2018. Thickness dependency of mechanical properties of laser-sintered polyamide lightweight structures. Addit. Manuf. 23. https://doi.org/10.1016/j.addma.2018.06.018.

van Aarle, W., Palenstijn, W.J., Cant, J., Janssens, E., Bleichrodt, F., Dabravolski, A., De Beenhouwer, J., Joost Batenburg, K., Sijbers, J., 2016. Fast and flexible X-ray tomography using the ASTRA toolbox. Opt. Express 24. https://doi.org/10.1364/oe.24.025129.

Viccica, M., Galati, M., Calignano, F., Iuliano, L., 2022. Design, additive manufacturing, and characterisation of a three-dimensional cross-based fractal structure for shock absorption. Thin-Walled Struct. 181, 110106. https://doi.org/10.1016/J.TWS.2022.110106.

Wang, M., Li, H.Q., Lou, D.J., Qin, C.X., Jiang, J., Fang, X.Y., Guo, Y.B., 2019. Microstructure anisotropy and its implication in mechanical properties of biomedical titanium alloy processed by electron beam melting. Mater. Sci. Eng. A 743. https://doi.org/10.1016/j.msea.2018.11.038.